Poly(2-ethyl-2-oxazoline) coating of additively manufactured biodegradable porous iron

Putra, N. E.; Tigrine, A.; Aksakal, S.; de la Rosa, V. R.; Taheri, P.; Fratila-Apachitei, L. E.; Mol, J. M.C.; Zhou, J.; Zadpoor, A. A.

DOI
10.1016/j.msec.2021.112617

Publication date
2022

Document Version
Final published version

Published in
Materials Science and Engineering C

Citation (APA)
Putra, N. E., Tigrine, A., Aksakal, S., de la Rosa, V. R., Taheri, P., Fratila-Apachitei, L. E., Mol, J. M. C., Zhou, J., & Zadpoor, A. A. (2022). Poly(2-ethyl-2-oxazoline) coating of additively manufactured biodegradable porous iron. *Materials Science and Engineering C*, *133*, Article 112617. https://doi.org/10.1016/j.msec.2021.112617

Biomaterials Advances 133 (2022) 112617

Contents lists available at ScienceDirect

Biomaterials Advances

journal homepage: www.elsevier.com/locate/bioadv

Poly(2-ethyl-2-oxazoline) coating of additively manufactured biodegradable porous iron

N.E. Putra [a,*], A. Tigrine [b], S. Aksakal [b], V.R. de la Rosa [b], P. Taheri [c], L.E. Fratila-Apachitei [a], J.M.C. Mol [c], J. Zhou [a], A.A. Zadpoor [a]

[a] Department of Biomechanical Engineering, Faculty of Mechanical, Maritime, and Materials Engineering, Delft University of Technology, Mekelweg 2, 2628 CD Delft, the Netherlands
[b] AVROXA BV, Technologiepark-Zwijnaarde 82, 9052 Ghent, Belgium
[c] Department of Materials Science and Engineering, Faculty of Mechanical, Maritime, and Materials Engineering, Delft University of Technology, Mekelweg 2, 2628 CD Delft, the Netherlands

ARTICLE INFO

Keywords:
Extrusion-based 3D printing
Biodegradable
iron
Scaffold
Bone substitution
Poly(2-ethyl-2-oxazoline) coating

ABSTRACT

Additively manufacturing of porous iron offers a unique opportunity to increase its biodegradation rate by taking advantage of arbitrarily complex porous structures. Nevertheless, achieving the required biodegradation profile remains challenging due to the natural passivation of iron that decrease the biodegradation rate. Moreover, the biocompatibility of iron is reported to be limited. Here, we address both challenges by applying poly(2-ethyl-2-oxazoline) coating to extrusion-based 3D printed porous iron. We characterized the specimens by performing *in vitro* biodegradation, electrochemical measurements, time-dependent mechanical tests, and *in vitro* cytocompatibility assays. The coated porous iron exhibited a biodegradation rate that was 2.6× higher than that of non-coated counterpart and maintained the bone-mimicking mechanical properties throughout biodegradation. Despite the formation of dense biodegradation products, the coating ensured a relatively stable biodegradation (*i.e.*, 17% reduction in the degradation rate between days 14 and 28) as compared to that of non-coated specimens (*i.e.*, 43% drop). Furthermore, the coating could be identified even after biodegradation, demonstrating the longevity of the coating. Finally, the coated specimens significantly increased the viability and supported the attachment and growth of preosteoblasts. Our results demonstrate the great potential of poly(2-ethyl-2-oxazoline) coating for addressing the multiple challenges associated with the clinical adoption of porous iron.

1. Introduction

Over the past decade, iron-based scaffolds have been developed as a new class of biodegradable materials to fulfil the requirements of temporary orthopedic implants [1]. Iron and its alloys possess higher mechanical properties than most of other biodegradable materials, thereby offering the potential of meeting the requirements for load-bearing applications, in which physiological loading, biodegradation, and bone regeneration occur harmoniously [2]. The development of iron-based biomaterials, however, remains challenging due to their too low rates of biodegradation [3]. The biodegradation process of iron results in the formation of corrosion products (*e.g.*, iron hydroxides and iron phosphate) that hinder oxygen transport to iron in the subsurface [4], thereby slowing down the continued corrosion of iron. The other major challenge in the use of iron-based biomaterials is their limited cytocompatibility [5]. While several studies have tried to address the abovementioned challenges [6,7], they remain unresolved. Alloying iron with lower standard electrode potential elements is one of the most widely used strategies [7–9]. Alternatively, adding alloying elements to iron can generate new phases that induce local galvanic corrosion and, thus, speed up its corrosion [7,9]. However, such alloying elements can be even more cytotoxic than iron.

The recent advances in additive manufacturing (AM) techniques, such as selective laser melting (SLM) [10–12] and extrusion-based 3D printing [13], have enabled the fabrication of iron-based biomaterials with arbitrarily complex hierarchical geometries and fully interconnected pores. A highly porous structure has much large surface area than its solid counterpart, favoring accelerated biodegradation of iron. However, this approach may become less effective over time for iron, as dense passive biodegradation products gradually form.

Biofunctionalization with polymer or bioceramic coatings is another strategy to both alter the biodegradation behavior of iron and provide osteogenic properties [14,15]. While the addition of bioceramics induces osteogenic properties, these coatings tend to reduce the biodegradation rate of iron due to their stable nature [16–19]. Polymer coatings (*e.g.*, based on polylactic acid (PLA) [20–22], poly(lactic-*co*-glycolic acid) (PLGA) [23], polyethylene glycol (PEG) [24], and polyethyleneimine (PEI) [25]) enhance the biodegradation of iron too [21–25]. Moreover, these coatings have been shown to be cytocompatible for various cell types [26–28].

Gradual hydrolyzation of biodegradable polymer coatings (*i.e.*, PLA and PLGA) creates an acidic environment [24] that accelerates the dissolution

* Corresponding author.
E-mail address: n.e.putra@tudelft.nl (N.E. Putra).

http://dx.doi.org/10.1016/j.msec.2021.112617
Received 15 October 2021; Received in revised form 6 December 2021; Accepted 13 December 2021
Available online 16 December 2021

of biodegradation products, thereby exposing more bare iron surface to biodegradation [21–23]. Although PEG is often regarded as a non-biodegradable polymer, it is known to be sensitive to oxidative degradation due to its polyether backbone [29]. Indeed, the coating layer should not biodegrade too quickly in order to make sure it can foster continuous transport of metallic ions out of the bulk material, while preventing the strong adhesion of degradation products that would otherwise inhibit further corrosion of iron.

Recently, poly(2-alkyl/aryl-2-oxazoline)-based polymers (PAOx) have received much attention as PEG alternatives in biomedical applications [30,31]. Unlike PEG, PAOx possess a tertiary amide backbone, which makes the polymer highly stable under biologically relevant conditions [32,33]. Moreover, PAOx are highly versatile, offering a broad range of end-group and side-chain functionalization possibilities attainable through copolymerization [30]. Poly(2-ethyl-2-oxazoline) (PEtOx) is the most investigated PAOx derivative, due to its similar hydrophilicity to PEG and balanced amphiphilicity [31]. PEtOx has demonstrated great potential for application in tissue regeneration and as the basis of a wide variety of drug delivery systems [34–36]. However, it has never been applied for the bio-functionalization of AM porous iron.

We have recently demonstrated how extrusion-based 3D printing can deliver hierarchical porous iron with much enlarged surface area (to improve their biodegradability) and bone-mimicking mechanical properties [13]. Here, we combined this fabrication method with PEtOx coatings to develop multifunctional porous iron scaffolds, which were then thoroughly characterized by performing *in vitro* biodegradation experiments, electrochemical measurements, time-dependent measurements of mechanical properties, and *in vitro* cytocompatibility assays.

2. Materials and methods

2.1. 3D printing of porous iron scaffolds

Porous iron scaffolds with a diameter of □ = 10 mm and a height of h = 10.5 mm were manufactured using extrusion-based 3D printing, followed by debinding and sintering, as described in detail elsewhere [13]. Briefly, an iron ink was prepared using a pure iron powder (Material Technology Innovations Co. Ltd., China) and a hydroxypropyl methylcellulose (hypromellose, $M_w \sim 86$ kDa, Sigma Aldrich, Germany) aqueous solution. The pure iron powder had the following characteristics: purity = 99.88%; morphology = spherical; particle size distribution: D_{10} = 25.85 μm, D_{50} = 39.93 μm, and D_{90} = 53.73 μm. The iron ink was extruded using a 3D printer (BioScaffolder 3.2, GeSiM Bioinstruments and Microfluidics, Germany) to create a 0° and 90° alternating pattern with a strut size of 410 μm and a strut spacing of 400 μm, through which the scaffolds were fabricated with a design density of 50% and a design surface area of 40.4 cm^2 (Fig. 1). The 3D printed pure iron scaffolds were subjected to a debinding process at 350 °C and were sintered at 1200 °C under pure argon flow in a tube furnace (Carbolite Gero Ltd., UK). The sintered iron scaffolds were then ultrasonically cleaned in isopropyl alcohol for 15 min prior to coating. These scaffolds will hereafter be referred to as non-coated iron.

2.2. Synthesis and characterization of poly(2-ethyl-2-oxazoline)

We added 2.02 mol of distilled 2-ethyl-2-oxazoline (203.6 mL, Polymer Chemistry Innovations, Arizona, USA), 300.7 mL ethyl acetate (purity 99.9%, extra dry, Fisher Scientific), and 20.19 mmol of distilled methyl p-toluenesulfonate (3.055 mL, purity 98%, Sigma Aldrich) to a 1-L Schott bottle that was equipped with a magnetic stirrer and was sealed in a glovebox under an inert and dry atmosphere. The polymerization mixture was heated for 21 h at 60 °C in an oil bath, followed by a cool-down step to reach the room temperature. The polymer was terminated in the glovebox with 22.21 mmol, 9.34 mL tetramethylammonium hydroxide solution (25 wt% in methanol) [37]. The reaction was filtered and subsequently concentrated *in vacuo*. The residue was dissolved in deionized water and was purified by dialysis in water, followed by freeze-drying to yield (114 g, 57%) a white solid.

The molar mass (M_n) values of the PEtOx polymer were characterized using size-exclusion chromatography (SEC, Agilent 1260-series high-performance liquid chromatography system, USA) and was calculated against the linear PEtOx standards (Avroxa, Belgium). The dispersity (Đ) values were calculated against the linear PMMA standard (Polymer Standard Service). In addition, ^{1}H nuclear magnetic resonance (NMR) analysis was conducted using a Bruker Avance 400 spectrometer (400 MHz, USA) to confirm the composition of the PEtOx polymer (Fig. S2).

2.3. Surface biofunctionalization

The PEtOx-OH terminated polymer (purity >95%, $M_{n,\ theoretical}$ = 9.9 kDa, $M_{n,\ SEC}$ = 9.7 kDa (PEtOx standard calibration), and Đ = 1.10, Fig. S3) was dissolved in 96% ethanol with a concentration of 10% *w/v*. The iron scaffolds were immersed into the PEtOx-OH solution. A vacuum pressure of 7 kPa was applied for 15 min to infiltrate the polymer into the open pores of the scaffolds. After that, the scaffolds were dried overnight. These scaffolds will hereafter be referred to as PEtOx-coated iron (Fig. 1).

2.4. Characterization of the surface-biofunctionalized scaffolds

The morphologies of the non-coated iron and PEtOx-coated iron were examined using a scanning electron microscope (SEM, JEOL JSM-IT100, Japan), and both the strut sizes and strut spacings were measured. The chemical composition of the coating was analyzed using X-ray energy dispersive spectroscopy (EDS, JEOL JSM-IT100, Japan). The cross-section of the PEtOx-coated iron was imaged using the same SEM and the coating thickness was measured. The regions of interest on the cross-sections of the struts were determined and the pore area was selected using ImageJ (NIH, USA). The solid fraction, S, of the struts was calculated as:

$$S = \left(1 - \frac{Pore\ area}{Total\ area\ of\ ROI}\right) \times 100\% \quad (1)$$

In addition, the chemistry of the PEtOx-OH polymer and that of the PEtOx-coated iron specimen were determined using a Fourier-transform infrared spectroscope (FTIR, Nicolet iS50 FT-IR, Thermo Scientific, USA) equipped

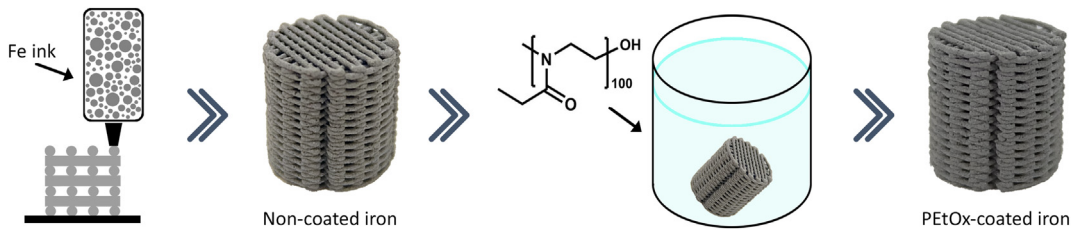

Fig. 1. Illustrations of extrusion-based 3D printing, non-coated iron scaffolds, the process of coating the porous iron scaffolds in a PEtOx-OH solution, and a PEtOx-coated iron specimen.

with built-in attenuated total reflection (ATR) and a liquid nitrogen-cooled mercury-cadmium-telluride detector. The phase composition of the PEtOx-coated iron specimen was identified using an X-ray diffractometer (XRD, Bruker D8 Advance diffractometer in the Bragg-Brentano geometry). The XRD was equipped with a graphite monochromator and a Lynxeye position-sensitive detector and operated using Cu Kα radiation at 45 kV and 40 mA and with a step size of 0.030° and a counting time of 2 s per step. The X-ray datasets were analyzed using the Diffrac Suite.EVA v5.2 software (Bruker, USA).

2.5. Characterization of the porosity of the scaffolds

The non-coated iron and PEtOx-coated iron scaffolds were weighed to determine the increase in their mass due to coating. A dry weighing method was used to obtain the absolute porosity values:

$$\varphi_p = \left(1 - \frac{m_p/\rho_{ink}}{V_{bulk}}\right) \times 100\% \quad (2)$$

$$\varphi_s = \left(1 - \frac{m_s/\rho_{Fe}}{V_{bulk}}\right) \times 100\% \quad (3)$$

$$\varphi_c = \left(1 - \frac{m_c/\rho_{PEtOx\ -\ Fe}}{V_{bulk}}\right) \times 100\% \quad (4)$$

where φ is the absolute porosity [%] and m is the mass [g] of the as printed (subscript = p), as sintered (subscript = s), and as-coated (subscript = c) specimens. In addition, ρ_{ink} is the density of the iron ink (*i.e.*, 4.41 g/cm^3), ρ_{Fe} is the theoretical density of iron (*i.e.*, 7.87 g/cm^3), $\rho_{PEtOx\text{-}Fe}$ is the density of PEtOx-coated iron scaffold (*i.e.*, 6.41 g/cm^3), and V_{bulk} is the bulk volume [cm^3] of the specimens.

Based on the ASTM standard B963-13 [38], the interconnected porosity values of the non-coated iron and PEtOx-coated iron scaffolds were determined as:

$$\varphi_i = \left(\frac{\rho_e}{\rho_o} \times \frac{m_{ao} - m_a}{m_{ao} - m_{eo}}\right) \times 100\% \quad (5)$$

where φ_i is the interconnected porosity [%], ρ_e is the density of ethanol (*i.e.*, 0.789 g/cm^3), ρ_o is the density of oil (*i.e.*, 0.919 g/cm^3), m_a is the mass [g] of the scaffold weighed in air, and m_{ao} and m_{eo} are the masses [g] of the specimens impregnated with oil and weighed in air and ethanol, respectively.

2.6. In vitro biodegradation characterization

2.6.1. Immersion tests and biodegradation product characterization

The PEtOx-coated iron scaffolds were immersed in the revised simulated body fluid (r-SBF, static environment) whose ion concentrations are given in Table 1 in comparison with those of the total human blood plasma [39]. The environmental conditions were as follows: pH = 7.40, temperature = 37 ± 0.5 °C, 5% CO_2, and relative humidity (RH) = 95%. There was 6.7 mL of medium available for every 1 cm^2 of the scaffold surface area [40]. The immersion continued uninterrupted for 2, 7, 14, and 28 days (in triplicate). The non-coated iron was included as the control group. The pH values of the fluid were measured both close to the specimens and far from them using a pH electrode (InLab Expert Pro-ISM, METTLER TOLEDO, Switzerland). In addition, the concentrations of soluble iron, calcium, and phosphate ions were measured using an inductively coupled plasma optical emission spectroscope ICP-OES (iCAP 6500 Duo, Thermo Scientific, USA).

Table 1
The ion concentrations of the r-SBF medium in comparison with those of the total human blood plasma [39].

Ion	Concentration (mM)	
	in total human blood plasma	in r-SBF
Na^+	142.0	142.0
K^+	5.0	5.0
Mg^{2+}	1.5	1.5
Ca^{2+}	2.5	2.5
Cl^-	103.0	103.0
HCO_3^-	27.0	27.0
HPO_4^{2-}	1.0	1.0
SO_4^{2-}	0.5	0.5

At selected time points (*i.e.*, 7, 14, and 28 d), the morphologies of the biodegradation products on the periphery of the PEtOx-coated iron were observed using a SEM (JEOL JSM-IT100, Japan), and the main elemental compositions of the biodegradation products were determined using EDS (JEOL JSM-IT100, Japan). The phase compositions of the biodegradation products of the PEtOx-coated iron after 28 days of immersion were determined using XRD (D8 Advance, Bruker, USA). To examine the remaining PEtOx coating layer after 28 days of immersion, the biodegraded scaffolds were gently shaken during retrieval from the immersion medium to remove loosely attached peripheral biodegradation products. The surface of the scaffolds beneath the peripheral degradation products was investigated using SEM and EDS. In addition, the biodegraded scaffolds were cut through a transverse plane at the center of the scaffold, the cross section was polished, and the biodegradation products formed inside the struts (*i.e.*, in the micropores between sintered Fe powder particles) were examined. The remaining solid fraction in the PEtOx-coated iron struts after 28 days of immersion was calculated using ImageJ (NIH, USA) and Eq. (1).

Furthermore, the mass losses of the non-coated iron and PEtOx-coated iron scaffolds were calculated after the dissolution of the biodegradation products of the scaffolds in 6 M hydrochloric acid supplemented with 0.025 M hexamethylene tetramine, following the ASTM standard G1-03 [41]. From the mass loss values, the average corrosion rate was calculated, based on the ASTM standard G31-72 [42], as:

$$CR\ [mm/year] = 8.76 \times 10^4 \times \frac{m}{A \times t \times \rho} \quad (6)$$

where ρ is the theoretical density of iron (g/cm^3), t is the duration of immersion [h], A is the surface area of the scaffold [cm^2] calculated based on the initial scaffold design value, and m is the mass loss [g].

2.6.2. Electrochemical measurements

The electrochemical responses of the PEtOx-coated iron scaffolds during biodegradation were measured in r-SBF (temperature = 37 ± 0.5 °C and pH = 7.40) using a three-electrode setup consisting of an Ag/AgCl electrode (the reference), a graphite rod (the counter electrode), and the test specimen (the working electrode) that was connected to a Bio-Logic SP-200 potentiostat (Bio-Logic Science Instruments, France). The PEtOx-coated iron specimens (in triplicate, for every time point) were partially embedded in an acrylic resin, were cleaned in isopropyl alcohol, and were thoroughly dried prior to electrochemical measurements. First, the three-electrode system was stabilized for 60 min to reach a steady open circuit potential (OCP). Subsequently, linear polarization resistance (LPR) and electrochemical impedance spectroscopy (EIS) measurements were performed at various time points till 28 days of immersion. In the LPR tests, a scan rate of 0.167 mV/s from −25 to +25 mV *versus* OCP was applied. For the LPR measurements, the non-coated specimens were included as the control group. In the EIS tests, a frequency range of 100 kHz to 10 mHz and a sinusoidal amplitude of 10 mV *versus* OCP was used. The resulting Nyquist and Bode curves were plotted and analyzed. The Nyquist impedance data points at low frequencies (*i.e.*, at 0.2 to 0.05 Hz) were linearly extrapolated and the angles between the line and x-axis were determined.

2.7. Mechanical tests

Uniaxial compressive mechanical properties of the PEtOx-coated iron scaffolds and the specimens retrieved at multiple time points (*i.e.*, after 7, 14, and 28 days of immersion) were determined using a mechanical testing

machine (100 kN load cell, Zwick Z100, Germany). Displacement-controlled tests (in triplicate for every time point) were conducted using a crosshead speed of 3 mm/min, following the ISO standard 13314:2011 [43]. The elastic modulus was determined as the slope of the first linear region of the stress-strain curve. The yield strength value was determined as the intersection of the stress-strain curve with the line representing the 0.2% offset strain, which was drawn in parallel with the first linear region of the curve.

2.8. Cytocompatibility evaluation

2.8.1. Preculture of cells

Mouse preosteoblasts (MC3T3-E1, Sigma Aldrich, Germany) were precultured for 7 days in a cell culture incubator with the following conditions: temperature = 37 ± 0.5 °C, RH = 95%, and 5% CO_2. A cell culture medium consisting of the α-minimum essential medium (α-MEM, Thermo Fisher Scientific, USA) without ascorbic acid but supplemented with 10% fetal bovine serum (FBS, Thermo Fisher Scientific, USA) and 1% penicillin/streptomycin (p/s, Thermo Fisher Scientific, USA) was used. The same cell culture medium was used in the preparation of iron extracts and for the cell culture assays.

2.8.2. Preparation of the iron extracts

The required extracts were obtained from the PEtOx-coated iron scaffolds (sizes: □ = 9.75 mm and h = 10.25 mm) after 72 h of incubation [44] in the cell culture medium, with a sample surface area to the medium volume ratio of 5 cm^2/mL (100% extract). Diluted versions of the extracts (*i.e.*, 75%, 50%, or 25%) were then prepared by adding the cell culture medium. The concentration of iron ions in the 100% extract was measured using ICP-OES (iCAP 6500 Duo, Thermo Scientific, USA). Prior to the tests, the iron extracts were filtered (pore size = 0.22 μm, Merck Millipore, Germany) and were stored at 4 °C.

2.8.3. Indirect test: PrestoBlue assay

Preosteoblasts MC3T3-E1 (1×10^4 cells) were cultured in 200 μL of the PEtOx-coated iron extract with various degrees of dilution. The PrestoBlue assay (as described elsewhere [13]) was utilized to evaluate the metabolic activity of the cells. The preosteoblasts were cultured in 48-well plates and the tests were conducted in triplicate after 1, 3, and 7 days of culture. The preosteoblasts cultured in the cell culture medium served as the negative control. After cell culture, the PrestoBlue reagent (Thermo Fisher Scientific, USA) was added to the wells and the absorbance values were measured using a Victor X3 Wallac plate reader (PerkinElmer, USA). The metabolic activity of the preosteoblasts was calculated as:

$$\textit{Metabolic activity}\ [\%] = \frac{\textit{Absorbance}\ (\textit{specimen})}{\textit{Absorbance}\ (\textit{negative control})} \times 100 \quad (7)$$

2.8.4. Direct assays: viable cell count and live/dead staining

Preosteoblasts MC3T3-E1 (5×10^4 cells) were seeded onto the PEtOx-coated iron (sizes: □ = 9.75 mm and h = 1.3 mm) and were cultured in 6-well plates with 8 mL of the cell culture medium. The Trypan blue reagent (Bio-Rad, USA) and cell counting methods (as described elsewhere [13]) were utilized to determine the number of viable cells after cell culture for 1, 4, 7, 14, and 28 days. The non-coated specimens were included as the control group, and the tests were performed in triplicate at every time point. After 4, 7, and 14 days of culture, the preosteoblasts were stained using calcein and ethidium homodimer-1 (Thermo Fisher Scientific, USA). Furthermore, the morphology of the preosteoblasts present on the scaffolds was examined with SEM after 14 days of culture.

2.9. Statistical analysis

The statistical analysis was carried out using two-way ANOVA and Tukey multiple comparison *post hoc* test for PrestoBlue and Trypan blue assays in the cell culture experiments (**** = $p < 0.0001$, *** = $p < 0.001$, ** = $p < 0.01$, and * = $p < 0.05$, *n.s.* = not significant).

3. Results

3.1. Morphological and chemical characterization of the scaffolds

The extrusion-based 3D printed porous iron scaffolds demonstrated a 0° and 90° lay-down pattern, essentially replicating the design (Fig. 2a-c). Their dimensions were 9.75 ± 0.03 mm in diameter and 10.24 ± 0.02 mm in height. Their actual strut size was 411 ± 6 μm with an actual strut spacing of 399 ± 6 μm and an actual interconnected porosity of 67 ± 2% (Table 2). After PEtOx coating, the porous structure and the strut geometry of the scaffolds remained almost unchanged (Fig. 2d). A relatively uniform layer of PEtOx coating covered the surface of partially sintered iron powder particles (Fig. 2e), and contained Fe, C, O, and N (Fig. 2f). The coating was very thin with a thickness of 2.0 ± 0.5 μm (Fig. 2g). The dimensions of the coated scaffolds hardly changed, with a diameter of 9.75 ± 0.02 mm and a height of 10.25 ± 0.01 mm, but the coating moderately altered the strut width and strut spacing to 413 ± 4 μm and 397 ± 5 μm, respectively. In addition, the PEtOx-coated iron scaffolds had a lower interconnected porosity, (*i.e.*, 61 ± 1%) (Table 2) and an increased solid fraction (*i.e.*, 94 ± 4%) than the non-coated iron. The XRD analysis of the PEtOx-coated iron scaffold revealed the presence of the α-iron phase, confirming that the coating process did not induce oxidation and did not affect the purity of the base material (Fig. S1). The FTIR spectrum of the PEtOx-coated iron scaffolds showed various transmittance bands that are similar to those of the PEtOx-OH polymer, but with lower intensities (Fig. 2h). The FTIR valleys at 1061 cm^{-1}, 1194 cm^{-1}, and 1238 cm^{-1} indicated the presence of CC stretching, while the bands at 1322 cm^{-1}, 1374 cm^{-1}, and 1470 cm^{-1} indicated the presence of CH bending [45]. The FTIR bands at 1419 cm^{-1} and 1625 cm^{-1} were respectively attributed to CH_3 bending and CO (amide) stretching [46]. On the PEtOx-coated iron scaffolds, the CO (amide) valley was shifted to 1628 cm^{-1}. Moreover, the transmittance bands at 2874 cm^{-1}, 2939 cm^{-1} and 2977 cm^{-1} suggested the existence of CH_2 stretching [45,47]. The OH bonding at 3488 cm^{-1} on the PEtOx-OH polymer was attributed to the hydroxyl terminated feature of the polymer. On the other hand, the OH group appeared to be diminished on the PEtOx-coated iron scaffold.

3.2. In vitro biodegradation characteristics

Yellow-brownish biodegradation products appeared on the periphery of the PEtOx-coated iron scaffolds after 28 days of static *in vitro* immersion (Fig. 3a). At the 2nd day of immersion, the PEtOx-coated iron scaffolds exhibited a biodegradation rate of 0.32 ± 0.01 mm/y. At the 14th day of immersion, the biodegradation rate dropped to 0.16 ± 0.04 mm/y. Then, the rate of biodegradation continued to decline until it reached 0.13 ± 0.02 mm/y at the 28th day of immersion (Fig. 3b). On the other hand, the biodegradation rate of the non-coated iron specimens were 0.11 ± 0.03 mm/y at the 2nd day of immersion, which declined to 0.09 ± 0.02 mm/y at the 14th day of immersion and further dropped to 0.05 ± 0.03 mm/y at day 28 (Fig. 3b).

Throughout the *in vitro* biodegradation experiments, the pH values in the vicinity of the PEtOx-coated iron and the pH values distant from the scaffolds remained around 7.68 to 7.70, slightly higher than the values measured for the non-coated iron specimens (*i.e.*, 7.63). As the biodegradation experiments progressed, iron ions were continuously released to r-SBF (Fig. 3d). The iron ion concentration from the PEtOx-coated iron scaffolds was the highest on the 2nd day of immersion (*i.e.*, 2.26 ± 0.30 mg/L), while the iron ions released from the non-coated scaffolds gradually increased until the 14th day of immersion (*i.e.*, 0.67 ± 0.04 mg/L). Subsequently, the iron ion concentrations decreased until day 28 where they reached 0.11 ± 0.01 mg/L and 0.08 ± 0.05 mg/L for the PEtOx-coated iron and non-coated specimens, respectively. Meanwhile, the calcium and phosphate ions present in the immersion medium continuously decreased with time (Fig. 3e-f). The decrease in the phosphate ions was more pronounced in the case of the non-coated specimens than the PEtOx-coated iron scaffolds. In the case of the PEtOx-coated iron specimens, the measured

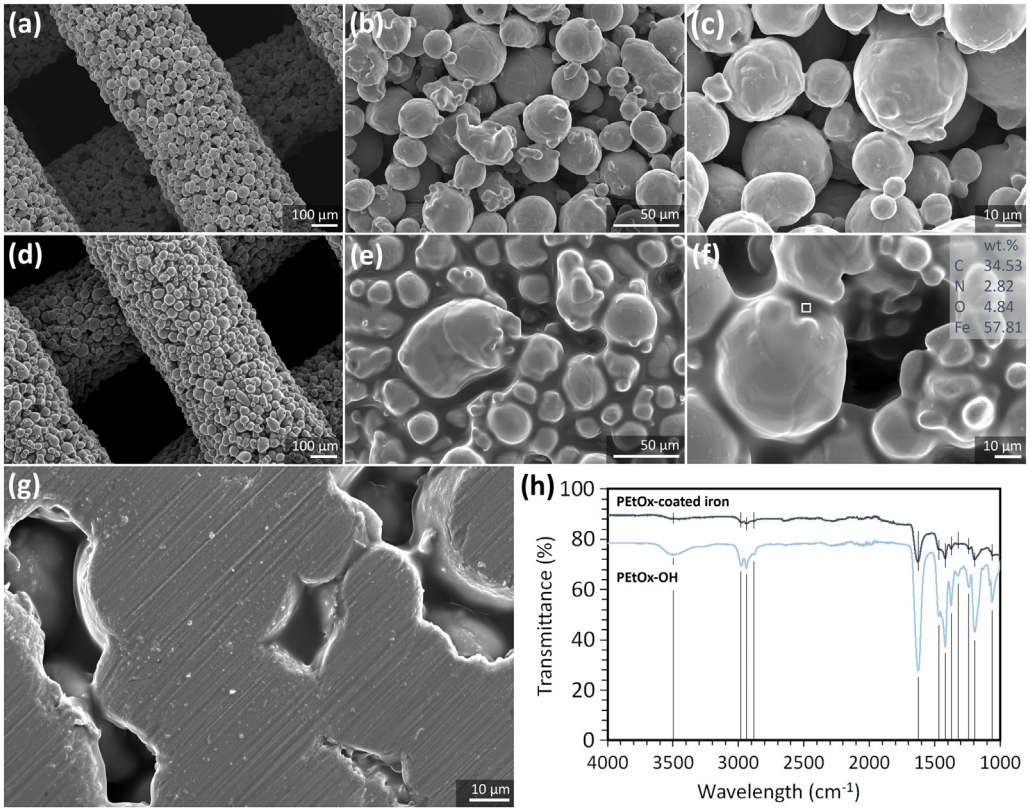

Fig. 2. The morphologies of (a, b, c) non-coated iron and (d, e, f) PEtOx-coated iron at different magnifications, (g) the cross-section of the PEtOx-coated iron scaffold struts, and (h) the FTIR graph of the PEtOx-OH polymer and PEtOx-coated porous iron specimens.

concentrations of phosphate ions were 85.3 ± 2.7 mg/L on day 2, 67.4 ± 1.1 mg/L on day 7, 31.7 ± 0.1 mg/L on day 14, and 5.2 ± 0.6 mg/L on day 28, while the phosphate ions concentrations associated with the non-coated specimens were 67.66 ± 2.3 mg/L on day 2, 32.74 ± 3.0 mg/L on day 7, 10.02 ± 2.2 mg/L on day 14, and 1.2 ± 0.3 mg/L on day 28.

3.3. Characteristics of the biodegradation products

After 28 days of *in vitro* immersion, the biodegradation products of the PEtOx-coated iron scaffolds at the periphery were identified as lepidocrocite (Fig. 3c) and a 78 ± 6% solid fraction of the PEtOx-coated iron specimens was retained. In addition, Fe and O appeared to be the main elements in the biodegradation products, along with C, Ca, P, Cl, S, and Mg (Fig. 4). The biodegradation product layer after 7 days of immersion was less compact than the layer formed at the later time points of immersion (*i.e.*, days 14 and 28, Fig. 4a-c). At the 7th day of immersion (Fig. 4a), the biodegradation products formed on the PEtOx-coated iron specimens were dense and granulated with two distinct chemical compositions: one containing C, O, S, Cl, Ca, P, and Fe (Fig. 4d) and the other being composed of Fe, Ca, P, and O (Fig. 4g). The detection of the latter suggested the formation of iron/calcium phosphate compounds. On days 14 and 28, the biodegradation products appeared to be denser (Fig. 4b-c). At a higher magnification, the morphology of the biodegradation products formed on the PEtOx-coated iron scaffolds appeared to be granulated with a variety of very fine porous features (Fig. 4e-f). On days 14 and 28, the chemical compositions of the biodegradation products (*i.e.*, C, O, Cl, Ca, P and Fe) were similar to those on day 7 with somewhat increased concentrations of calcium and phosphorus (Fig. 4h-i).

Underneath the peripheral layer of the biodegradation products (Fig. 5a-c), the interconnected porous struts of the PEtOx-coated iron scaffolds were still clearly discernible. The surface of the interconnected iron particles was also covered by the biodegradation products. EDS analysis on the biodegradation products revealed the presence of N together with C, O, Na, Cl, and Fe (Fig. 5a). The N content (in terms of mass percentage) was lower than its initial value (Fig. 2f). Interestingly, at different spots, N was found along with C, O, and Fe (Fig. 5b), corresponding to the same chemical composition as found in the initial PEtOx coating (Fig. 2f). Other spots on the periphery of the specimens exhibited biodegradation products with similar chemical compositions (Fig. 5c). At the center of the PEtOx-coated iron scaffolds, solid biodegradation products (containing Fe, Ca, C, and O) were observed in the interconnected micro-pores of the struts, suggesting the formation of iron/calcium carbonate compounds (Fig. 5d). However, only Fe and O were detected in the EDS map (Fig. 5e).

Table 2
Characteristics of the extrusion-based 3D printed porous iron and PEtOx-coated iron scaffolds.

Sample group	Strut width (μm)	Strut spacing (μm)	Absolute porosity (%)	Interconnected porosity (%)
Design	410	400	50	–
Non-coated iron	411 ± 6	399 ± 6	69 ± 1	67 ± 2
PEtOx-coated iron	412 ± 4	398 ± 5	62 ± 1	61 ± 1

3.4. Electrochemical measurements

Over the 28 days of *in vitro* biodegradation, the OCP value of the PEtOx-coated iron scaffolds only changed insignificantly (Fig. 6a). The average OCP value on the 2nd day of immersion was −674 ± 6 mV, which essentially stabilized at −670 ± 21 mV, −671 ± 28 mV, and −677 ± 38 mV, respectively, on days 7, 14, and 28. To the contrary, the average OCP value of the non-coated iron specimens increased significantly throughout the immersion period (Fig. 6a). The OCP values were −696 ± 5 mV on day 2, −677 ± 5 mV on day 7, −673 ± 1 mV on day 14, and −600 ± 65 mV

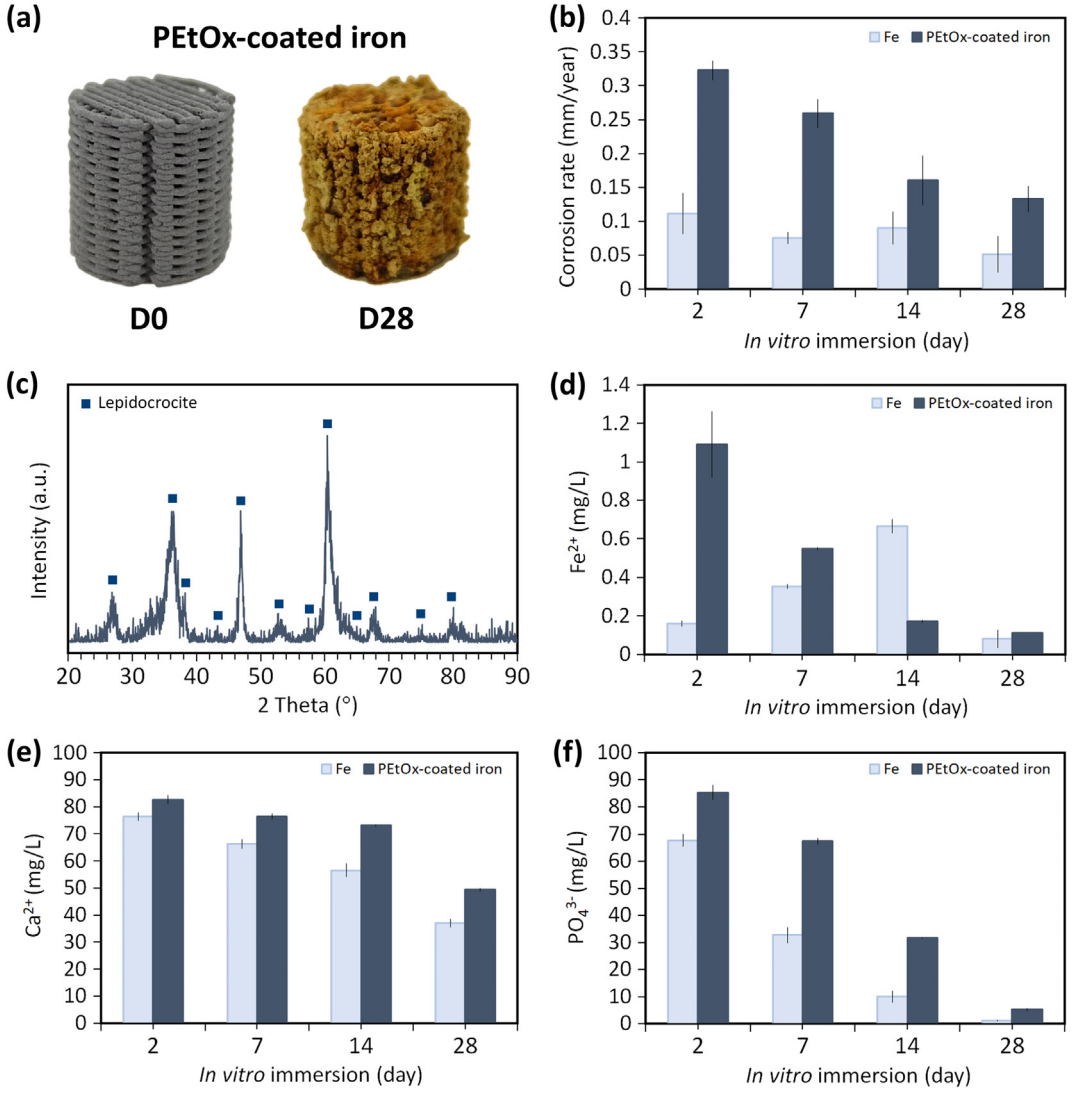

Fig. 3. The *in vitro* biodegradation of the PEtOx-coated iron scaffolds: (a) visualization of the specimens before and after 28 days of biodegradation, (b) corrosion rate, (c) the phase compositions of biodegradation products on day 28, and the time-dependent concentrations of (d) iron, (e) calcium, and (f) phosphate ions in the r-SBF solution during the *in vitro* biodegradation experiments.

on day 28. From the LPR tests of the PEtOx-coated iron specimens (Fig. 6b), the average polarization resistance (R_p) value on the 2nd day of immersion was 5.0 ± 0.7 kΩ·cm^2. Then, the R_p values increased to 5.7 ± 1.1 kΩ·cm^2, 6.6 ± 1.2 kΩ.cm^2, and 9.2 ± 3.2 kΩ·cm^2 on days 7, 14, and 28, respectively. For the non-coated iron specimens (Fig. 6b), the R_p values substantially increased from 3.3 ± 0.8 kΩ·cm^2 on day 2 to 29.9 ± 4.8 kΩ·cm^2 on day 28.

The impedance Nyquist plots of the PEtOx-coated iron scaffolds (EIS measurements) showed two distinct types of electrochemical responses: while a single semicircle can be observed on day 2 (Fig. 6c), an extra time constant (semicircle arc) was observed from day 7 to day 28 (Fig. 6d-e). The linear extrapolation line in the impedance Nyquist in the low frequency region (*i.e.*, 0.2 to 0.05 Hz) exhibited an angle of 43.4°, 42.7°, 41.7°, 44.8°, and 41.9° to the x-axis after 2, 7, 14, 21, and 28 d of immersion (Fig. 6c-e). The impedance magnitudes agreed with the R_p values. At a frequency of 0.01 Hz, the impedance Bode values of the PEtOx-coated iron specimens were 3.6 ± 0.3 kΩ·cm^2, 4.2 ± 0.6 kΩ·cm^2, 5.8 ± 0.9 kΩ·cm^2, and 7.9 ± 3.3 kΩ·cm^2, after 2, 7, 14, and 28 days of immersion, respectively (Fig. 6f). In the low frequency region (*e.g.*, 0.1 Hz), the Bode phase angle shifted towards a more positive value, from −38 ± 2° on day 2 to −22 ± 1° and −15 ± 5°, on days 14 and 28, respectively (Fig. 6g). In the higher frequency region (*e.g.*, at 10 kHz), however, the phase angle moved towards a more negative value from −1.1 ± 0.4° on day 2 to −17 ± 3° and −34 ± 10° on days 14 and 28, respectively.

3.5. Mechanical properties

The PEtOx-coated iron scaffolds exhibited smooth stress-strain curves under uniaxial compression even after *in vitro* biodegradation for 28 d. The stress-strain curves initiated with a linear elastic region, followed by a region with a less steep rate of stress increase resembling the plastic deformation region (Fig. 7a). The PEtOx-coated iron scaffolds were less ductile after biodegradation with the strain-to-failure dropping from 0.44 ± 0.07% to 0.35 ± 0.05% after 28 days of immersion. In addition, the PEtOx-coated iron specimens had a yield strength and an elastic modulus of 6.2 ± 0.8 MPa and 0.5 ± 0.09 GPa, respectively. On days 7 and 28, the yield strengths were 4.9 ± 1.4 MPa and 5.3 ± 1.0 MPa (Fig. 7b). At the same time points, the elastic moduli were 0.41 ± 0.08 GPa and 0.41 ± 0.06 GPa (Fig. 7b).

3.6. In vitro cytocompatibility

The MC3T3-E1 preosteoblasts cultured in 100% extracts associated with the PEtOx-coated specimens, containing 105.4 ± 5.7 mg/L iron ion,

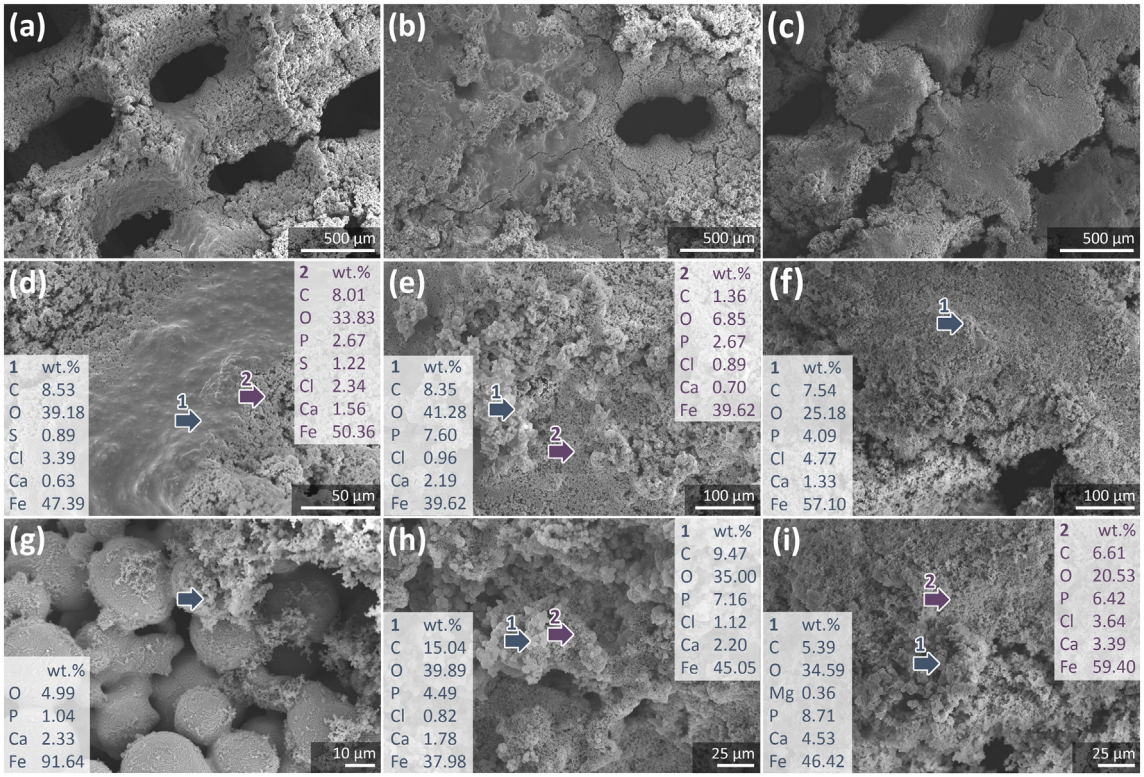

Fig. 4. The morphologies and chemical compositions of the biodegradation products on the periphery of the PEtOx-coated iron scaffolds after (a, d, g) 7, (b, e, h) 14, and (c, f, i) 28 days *in vitro* biodegradation. The arrow and number indicate the location of the EDS measurements.

exhibited a very low metabolic activity (*i.e.*, 13 ± 1% to 23 ± 3%) throughout the cell culture period of 7 days (Fig. 8a). The metabolic activity of the preosteoblasts improved to 43 ± 7% when cultured in 75% extract for 24 h. However, the value dropped to 25 ± 3% after 7 days of cell culture. At the 50% and 25% extracts, the metabolic activities of the cells were above 80% at all cell culture time points (Fig. 8a).

In addition, the direct culture of preosteoblasts on the PEtOx-coated iron scaffolds showed a significant increase in the number of cells after 7 days of culture ($p < 0.01$), which was maintained over the remaining culture period (Fig. 8b). The numbers of viable preosteoblasts counted on the PEtOx-coated iron scaffolds were higher at all the time points than those on the non-coated iron scaffolds (*i.e.*, $p < 0.01$ at day 4 and $p < 0.0001$ at the 7th, 14th, and 28th day, Fig. 8b). In agreement with the cell counting assay, the live/dead staining revealed more viable (green-stained) cells adhered on the PEtOx-coated iron than the non-coated scaffolds at all the time points. The number of nonviable (red-stained) cells on the non-coated iron increased from the 4th day to the 14th day of cell culture (Fig. 8c-e). However, the preosteoblasts remained viable (green-stained) on the PEtOx-coated iron scaffolds throughout the 14 days of cell culture period (Fig. 8g-i). On the non-coated

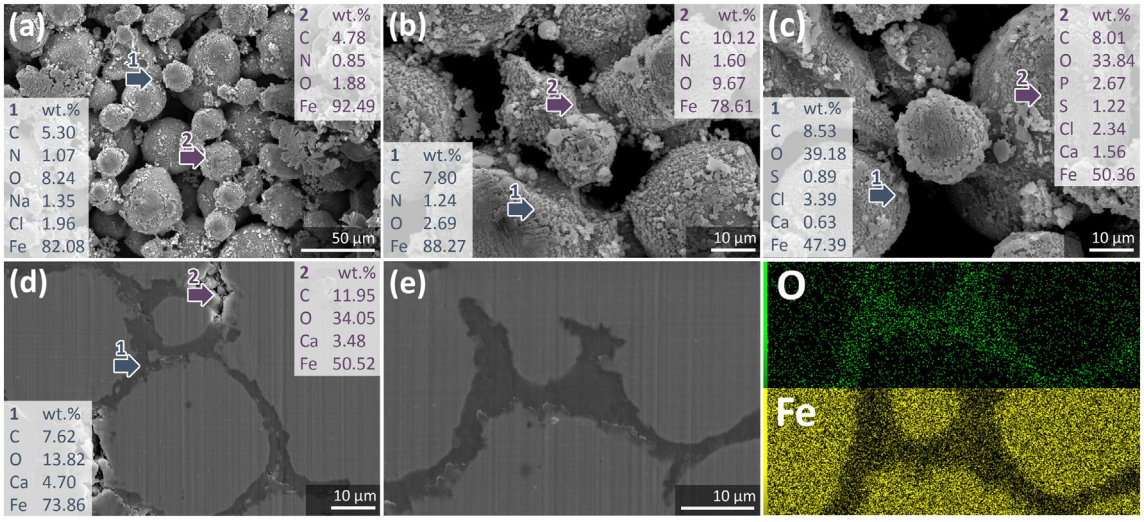

Fig. 5. The morphologies and chemical compositions of the biodegradation products of the PEtOx-coated iron scaffolds on day 28: (a, b, c) beneath the dense layer on the periphery imaged at different magnifications, (d, e) cross-section at the center, and (e) the EDS mapping on the cross-section. The arrows and numbers indicate the locations of the EDS measurements.

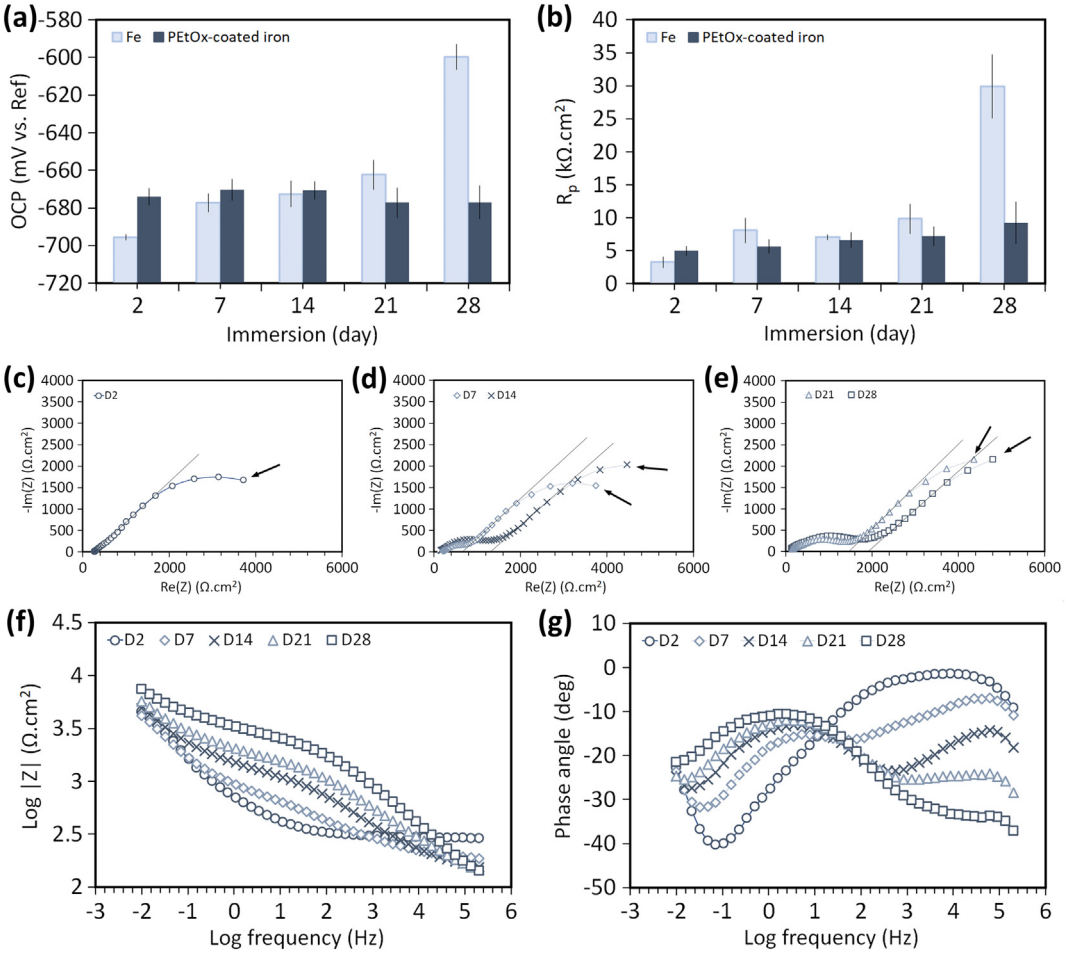

Fig. 6. The electrochemical measurements of the PEtOx-coated iron scaffolds during the biodegradation experiments: the evolution of the (a) OCP and (b) R_p values with time. (c, d, e) The Nyquist impedance curves at different time points. (f, g) The Bode impedance plot and phase angle values at different time points. The arrows indicate a specific frequency of 0.01 Hz. The lines indicate the linear extrapolation of Nyquist impedance at 0.2 to 0.05 Hz.

specimens, the morphology of the preosteoblasts was rounded and the cells were covered by particulate biodegradation products after 14 days of cell culture (Fig. 8f). On the contrary, the cells were spread and developed extended filopodia on the PEtOx-coated iron surface (Fig. 8j).

4. Discussion

The PEtOx coating applied to extrusion-based 3D printed iron scaffolds hold great promise, given that they have the potential to improve various properties of iron-based scaffolds, thereby enabling them to function as biodegradable bone substitutes. The favorable properties of PEtOx-coated porous iron include (i) an enhanced *in vitro* biodegradation rate (*i.e.*, 0.13 mm/y) that is 2.6 times higher than its non-coated counterpart, (ii) bone-mimicking mechanical properties [48] with a yield strength of 5.3–6.2 MPa and an elastic modulus of 0.41–0.46 GPa maintained even after 28 days of biodegradation, and (iii) enhanced cell viability and cell adhesion due to the presence of the PEtOx coating.

4.1. PEtOx coating on extrusion-based 3D printed porous iron scaffolds

The biomaterial developed here can be further improved using the other approaches available in the literature, such as alloying the base

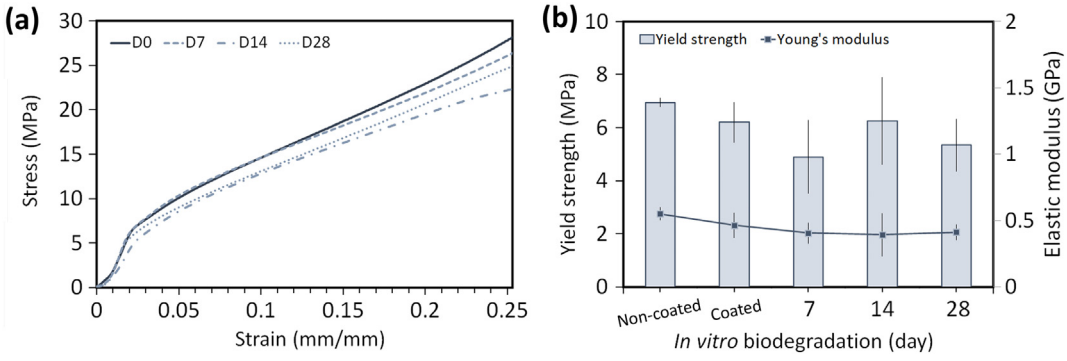

Fig. 7. The mechanical properties of the PEtOx-coated iron specimens: (a) stress-strain curves. Changes in the (b) yield strength and elastic modulus with biodegradation time.

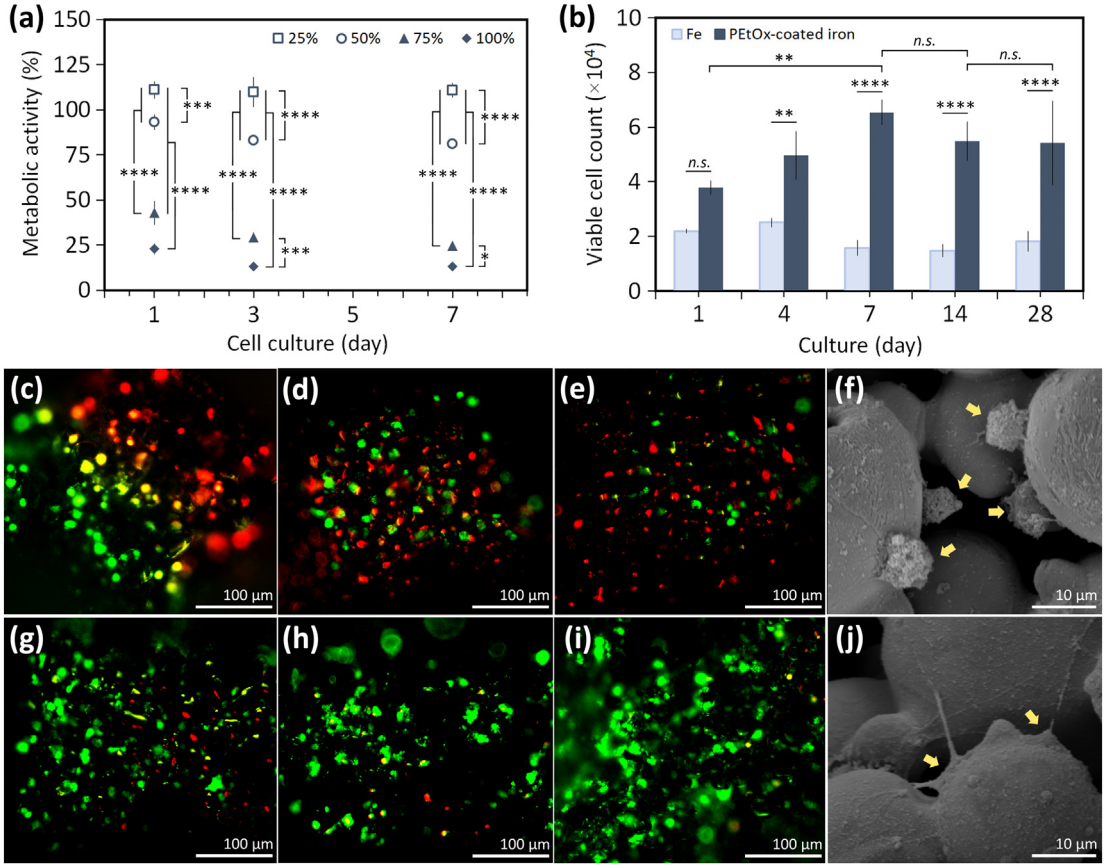

Fig. 8. The cytocompatibility of the PEtOx-coated iron scaffolds tested using MC3T3-E1 preosteoblasts: (a) the metabolic activity of the cells cultured with the extracts retrieved at different time points, (b) the viable cell counts over 28 days of culture. The live/dead staining of (c, d, e) the non-coated iron and (g, h, i) PEtOx-coated iron specimens after 4, 7, and 14 days of culture, and the typical morphology of the cells cultured in (f) the non-coated iron and (j) PEtOx-coated iron scaffolds (after 14 days of culture). **** = $p < 0.0001$, *** = $p < 0.001$, ** = $p < 0.01$, * = $p < 0.05$ and *n.s.* = *not significant.*

material prior to coating, fine-tuning the polymer concentration, and the application of other types of PAOx polymers. We immersed the 3D printed scaffolds in the polymeric solution, aided by a moderate vacuum. Similar to the dip coating technique, this is a reliable and straightforward method to create a thin and uniform layer on a material with a complex porous structure [49–51]. The use of vacuum was intended to ensure a thorough distribution of the polymer solution inside the open pores of the scaffolds. Vacuum has also been shown to improve the interfacial bonding of polymer and iron [23]. Aided by the negative pressure, the PEtOx polymer formed a relatively homogenous thin coating layer on the struts of the scaffolds (Fig. 2d). A relatively dense coating layer was observed on the necking of the iron powder particles (Fig. 2e-f). This can be attributed to the concave shape of the necking region that acts like a reservoir, holding extra polymer solution during the coating process. Importantly, the PEtOx layer on the surface of the porous iron scaffolds only marginally reduced the total porosity and preserved the high pore interconnectivity of the scaffolds (Table 2).

The PEtOx-OH polymer has several functional groups, including ethyl -CH_2-CH_3, carbonyl CO (tertiary amide) and a terminal hydroxyl group (OH) (Fig. 1). The small thickness of the coating meant that the overall intensities of the functional groups were decreased when measured on porous specimens. The valleys in the FTIR graph were, nevertheless, clearly visible, save for the diminished hydroxyl group, confirming the presence of the polymer on the iron surfaces (Fig. 2h). The flattened hydroxyl valleys in the FTIR graph of the coated scaffold suggested that this moiety participated in the polymer interaction with the iron surface. Besides that, a slight shift and decreased signal of the CO amide stretch band also implied that these amide groups took part in the interfacial bonding of the polymer to the iron surface [52]. From the FTIR peaks, some of the CO amide and other functional groups (*e.g.*, -CH_2-CH_3) were present on the PEtOx-coated iron scaffold surface. It is believed that these groups are responsible for the properties of the coating material. For example, the CO functional group is known for its hydrophilic behavior while the ethyl -CH_2-CH_3 functional group behaves more hydrophobically.

4.2. Biodegradation behavior

In general, scaffolds with a higher porosity (or larger surface area) are expected to degrade faster. That said, the surface of an implanted porous iron-based biomaterial will most likely be covered by the degradation products, passivating the material to some degree. Altering the surface chemistry of iron could be an effective approach to minimizing the adhesion of the corrosion products and facilitating continued biodegradation. Surface modification involving polymers has been reported in several studies and positive effects on the biodegradation behavior of iron-based biomaterials have been demonstrated [14,15].

The *in vitro* biodegradability of the PEtOx-coated iron (*i.e.*, 0.13 mm/y at day 28) was found to be similar to that of cross-rolled pure iron [53], but higher than SLM porous iron with 59% porosity [54]. The PEtOx coating increased the *in vitro* biodegradation rate by 2.6 times relative to the non-coated scaffolds. The improvement is comparable to that of other porous irons with polymer coatings [23,24]. For example, porous iron coated with PLGA has been reported to exhibit a biodegradation rate (day 28) that is 2.3 times higher than that of bare porous iron [23]. In addition, the biodegradation rate of a porous iron foam with a 5–15 wt% PEG coating has been found to be 1.4–2.3 times higher than that of a corresponding bare iron foam (day 28) [24].

As a result of biodegradation, iron ions were released, which then interacted with the other ionic compounds present in the r-SBF medium

and participated in the formation of the biodegradation products. The macro-scale morphology of the biodegradation products of the PEtOx-coated iron (Fig. 4c) appeared to be similar to that of the dense products observed on the surface of the non-coated iron. At the micro-scale, however, the morphology of the degradation products formed on the surface of the PEtOx-coated iron scaffolds was clearly porous (Fig. 4g-i), which is distinctly different from the products formed on the surface of the non-coated iron (as reported in our previous publication [13]). Such a porous morphology is believed to influence the biodegradation rate. From day 14 to 28, the *in vitro* biodegradation rate of the PEtOx-coated iron reduced only by 17%. During the same period, the biodegradability of the non-coated specimens decreased by 43%.

In addition to controlling the scaffold degradation rate, the PEtOx coating altered the chemistry of the iron-based biodegradation products too. The main phase of the PEtOx-coated iron biodegradation products was lepidocrocite. Such a phase has been observed on the biodegraded functionally graded porous iron [54] as well, resulting from the chemical reactions described in [55]. Interestingly, no iron phosphate or iron oxide products were formed on the coated scaffolds, unlike the biodegradation products on the non-coated specimens (as reported elsewhere [13]). The Fe-based degradation products containing phosphate have been reported to prevent corrosion from occurring further [56]. In addition, based on the EDS analysis, the biodegradation products of the PEtOx-coated iron at 14 and 28 days of *in vitro* immersion in r-SBF contained a larger variety of elements than those present on the non-coated iron (as reported elsewhere [13]). The absence of phosphate-based degradation products and the enriched elements in the chemical compositions of the biodegradation products are likely the reasons for the reduced passivation of the PEtOx-coated iron. Moreover, Ca and P precipitates were present at all time points (Fig. 4), which was not the case for the non-coated specimens. The precipitation of Ca/P elements correlated with the decreases in the concentrations of Ca^{2+} and PO_4^{3-} in the r-SBF (Fig. 3e-f). While Ca ions may be present both in Ca/P precipitates and in other compounds (*e.g.*, calcium carbonates), we may still assume that all Ca is used for the formation of the Ca/P precipitates. This simplifying assumption allows us to determine the Ca/P ratio. On day 7, the Ca/P ratio varied between 0.58 and 2.24. On days 14 and 28, the range of the determined Ca/P ratios narrowed to 0.26–0.40 and 0.32–0.53, respectively. Although the Ca/P ratios found do not correspond to the stoichiometry of hydroxyapatite (*i.e.*, $Ca/P = 1.67$), low Ca/P ratios (*e.g.*, 0.5) are reported to be beneficial for osteoblast viability, collagen synthesis, and alkaline phosphatase activity [57].

The biodegradation of polymers is known to create an acidic environment. For example, 7-day biodegradation of iron coated with PLGA resulted in a reduced pH value of 6.87 [23]. However, such a phenomenon was not observed in our study. The stable pH values around 7.70 during the biodegradation tests were in line with the expected stability of the polymer. From these, we can infer that the hydrolysis of the PEtOx polymer did not occur at all or at least to an extent that would affect the local and bulk pH. PAOx have been reported to be non-biodegradable [33] and to exhibit high stability in water [58], while being susceptible to oxidative degradation in the presence of hydrogen peroxide and transition metal ions that act as catalysts [59]. To the best of our knowledge, however, the degradation of PEtOx due to the presence of iron ions in a physiologically relevant environment has not been reported before. It is only known that the degradation of PEtOx is much slower in a Fe/H_2O_2 environment than in a Cu/H_2O_2 environment [60]. Interestingly, the chemical characteristics of PEtOx (*i.e.*, the N element present in the PEtOx backbone) could still be detected at several spots beneath the peripheral biodegradation products on the PEtOx-coated iron scaffolds after 28 days of biodegradation (Fig. 5). This finding is consistent with the observation that the pH remained relatively stable throughout the immersion period. In addition, we examined the surface characteristics and chemical composition of the PEtOx thin film after 7 days of immersion in the r-SBF medium (Fig. S4, Table S1). After exposure, the wt% value of the N element in the film was similar to the value prior to immersion. It confirmed the non-biodegradability of the polymer and indicated that the PEtOx polymer did not elute to the r-SBF medium. Moreover, the surface of the polymer film contained the Na, Cl, and K elements after immersion, clearly showing that diffusion of ionic compounds occurred in the polymer matrix. The absence of Ca/P-based implied that the precipitation only occurred due to the biodegradation of iron. However, no clear interface between PEtOx and iron was observed on the cross-section, likely because the thin polymer layer is not strong enough to survive the cutting and polishing processes of the biodegraded specimens. Even if the coating loses its integrity during the biodegradation process, its remnants may still assist the biodegradation of iron.

The electrochemical measurements of the PEtOx-coated iron demonstrated a relatively stable OCP trend over the 28 days of immersion (Fig. 6a), which was in contrast to the OCP trend of the non-coated iron. Over the immersion period, the R_p values obtained from LPR measurements of the PEtOx-coated iron scaffolds marginally increased but remained much lower than those of the non-coated pure iron (Fig. 6b). These electrochemical characteristics indicate that the stable PEtOx coating allows the corrosion of the porous iron to proceed further. Unlike other types of coatings, *e.g.*, those made of bioceramics [16–18], the effect of the PEtOx coating on the porous morphology of the biodegradation products (Fig. 4g-i) led to the reduced R_p values, thus enabling the sustained biodegradability of iron over time. The Nyquist plots coated iron specimens exhibited a single semicircle initially and then an extra time constant arc pattern at later times of exposure (Fig. 6c-e). As comparison, the Bode and Nyquist impedance of the non-coated iron specimens have been reported elsewhere [13]. Initially, the Nyquist semicircle arc of the PEtOx-coated iron (at day 2) had a much larger diameter than that of the non-coated iron. The larger Nyquist arc diameter indicates a higher polarization resistance value, which can be due to the presence of the PEtOx coating. This evidence is supported by the higher R_p value of the PEtOx-coated iron scaffolds during the first 2 days of immersion (Fig. 6a-b). The occurrence of an extra time constant in the Nyquist plot indicates active and diffusive biodegradation mechanisms occurring simultaneously with time [61]. The Nyquist impedance in the low frequency region (at 0.2 to 0.05 Hz) demonstrated a Warburg diffusion characteristics [62,63], indicated by the angle of the extrapolation line very close to 45° at all time points (Fig. 6c-e). The Warburg characteristic strongly suggests the biodegradation mechanism of the PEtOx-coated iron occurred by ion diffusion through the coating layer [63]. At the later time points, the Warburg effect was maintained due to the porous morphology of the biodegradation products of the coated scaffolds. Moreover, The Nyquist arcs of the PEtOx-coated iron scaffolds (from day 7 to day 28) had a similar diameter to the Nyquist arc of the non-coated iron on day 14, but were much smaller than the Nyquist arc of the non-coated iron on day 28. The Bode impedance modulus values of the PEtOx-coated iron scaffolds at 0.01 Hz displayed a similar trend to that of the R_p values, which were much lower, as compared to the values reported for the non-coated iron after 28 days of immersion. Altogether, the SEM and EDS analyses of the degradation products, the longevity of the coating layer, and the electrochemical responses indicate that the PEtOx coating promoted the biodegradation of iron largely *via* a diffusion mechanism through the polymer layer. The morphology and chemistry of the iron-based biodegradation products were altered due to the coating, thus inhibiting the biodegradation process to a lesser extent than the corresponding bare specimens. The exact mechanism operating during immersion in r-SBF still needs to be studied.

4.3. Mechanical properties

The strength and stiffness of biodegradable implants tend to reduce as the biodegradation progresses. The PEtOx-coated iron possessed bone-mimicking mechanical properties that fall into the range of the mechanical properties of trabecular bone (E = 0.02–2.0 GPa and σ_y = 0.1–30 MPa [48]). These properties were maintained even after 28 days of *in vitro* biodegradation (Fig. 7). The PEtOx coating layer did not significantly influence the yield strength and elastic modulus of the as-sintered specimens (Fig. 7b). During mechanical testing, the mechanical load was transferred across the iron scaffold as well as the interface between the iron and

PEtOx coating layer. The PEtOx polymer itself and the modified geometrical parameter (*i.e.*, the increased strut thickness and decreased porosity, Table 2) did not have any remarkable strengthening effect, which was ascribed to the small thickness of the coating layer and the amorphous and brittle nature of PEtOx [47].

As the biodegradation process progressed, the solid fraction of the scaffolds decreased, reducing the overall mechanical properties of the scaffolds. By day 28, the yield strength and elastic modulus of the PEtOx-coated iron scaffolds had decreased by 13.8% and 11.3%, respectively (Fig. 7b-c). In comparison, the mechanical integrity of biodegraded iron foams coated with PEG is reported to have been deteriorated after 6 weeks of *in vitro* biodegradation, although the biodegradation rate (*i.e.*, 0.04 to 0.06 mm/y) was lower than that of our PEtOx-coated iron scaffolds [64]. In the current study, however, the PEtOx-coated iron scaffolds maintained their structural integrity and a ductility >30% even after 28 days of *in vitro* biodegradation, suggesting that the coating did not adversely affect the biodegradation mechanism (*e.g.*, no severe localized corrosion attack). Such a ductile behavior improves resistance of the specimens against fatigue failure [65].

4.4. Cytocompatibility

The cytocompatibility of biodegradable metals strongly depends on the concentrations of the released metallic ions and the precipitated biodegradation products. The preosteoblasts cultured in the PEtOx-coated iron extracts (prepared from 72 h incubation) exhibited a very low metabolic activity (Fig. 8a). It has been reported that 53.2 to 88.5 mg/L of iron ion concentrations inhibit the preosteoblasts growth by 50% [66]. The iron ion concentration of the 100% PEtOx-coated iron extract was much higher than these values. The cytocompatibility level was, therefore, rank 4 (the lowest according to ISO 10993-5 [67]). A high iron ion concentration induces the formation of more reactive oxygen species, which causes oxidative stress on cells and tissue [68]. When the extracts were diluted to 50% or lower concentration, the preosteoblasts became metabolically active (80% or higher), indicating a very mild cytotoxic response (rank 1) [67].

In the direct cell culture assays, the PEtOx coating significantly enhanced the viability and growth of the cells, as revealed by the live/dead assay, SEM imaging of cell morphology and the cell counts at various culture times (Fig. 8b-j). These findings indicate that the coating supported the early response of preosteoblast cells with possible positive effects on the late cellular functions. When a polymer-coated iron scaffold is introduced to a protein-containing medium, the adsorption of proteins on the scaffold surface may occur, as observed in the case of PEI-coated iron in an albumin-containing medium [69]. Protein adsorption on surfaces creates a conditioned provisional layer favorable for cell attachment and has been reported to stimulate osteoblast adhesion [70,71]. At the same time, the released iron ions may interact with the proteins in the medium [72, 73], preventing the precipitation of iron-based degradation products and thereby maintaining a supportive interface for both cell response and biodegradation rate. Our short-term cytocompatibility results are similar to those available in the literature on polymer-coated iron scaffolds, including preosteoblasts MC3T3-E1 cultured on PLA-coated iron [20], human skin fibroblasts cultured on PLGA-coated iron [23], human dermal fibroblasts cultured on PEG-coated iron [74], and bone marrow stromal cells cultured on collagen-coated Fe30Mn [75]. To the best knowledge of the authors, *in vivo* study on the PEtOx polymer intended specifically for bone tissue regeneration has not yet been reported. Various POx-based polymers have however been studied *in vivo* with promising results [31], *e.g.*, for intraocular [76] or macromolecular antioxidant therapy [77] applications. The *in vitro* biological experiments performed in this research should be first extended further to assess the osteogenic potential of the coated scaffolds by investigating cell differentiation, extracellular matrix formation and mineralization, followed by additional assays to better understand the long-term performance of the developed biomaterials and then *in vivo* studies. Moreover, the addition of bioactive elements to iron-based biomaterials [78–80] is another suggested avenue for further research. Such additions could yield further improvements in the long-term biocompatibility of such biomaterials and may be used with or without biofunctional coatings.

5. Conclusions

We developed extrusion-based 3D printed porous iron scaffolds biofunctionalized with PEtOx polymer coatings and demonstrated their superior performance including an enhanced rate of biodegradation, bone-mimicking mechanical properties, and significantly enhanced cell viability. These properties underscore the potential of the developed biomaterials for application as bone substitutes. In summary, the PEtOx coating promoted the biodegradation of iron largely *via* a diffusion mechanism through the polymer layer. The coating also altered the morphology and chemistry of the iron-based biodegradation products, *i.e.*, making them porous, and prevented phosphate-based products from forming. The *in vitro* biodegradation rate of the PEtOx-coated iron scaffolds increased by 2.6 times, as compared to their non-coated counterparts, while improving cell viability and growth simultaneously. In addition, the PEtOx-coated iron maintained its bone-mimicking mechanical properties throughout the 28 days of the *in vitro* biodegradation experiments. Additional (*in vivo*) experiments are required for further evaluation of the developed biomaterials prior to clinical adoption.

CRediT authorship contribution statement

N.E. Putra: Conceptualization, Investigation, Methodology, Writing – Original Draft, Writing – Review & Editing, Visualization; **A. Tigrine**: Investigation, Methodology, Writing – Review & Editing; **S. Aksakal**: Investigation, Methodology, Writing – Review & Editing; **V.R. de la Rosa**: Methodology, Resources, Writing – Review & Editing, Supervision; **P. Taheri**: Methodology, Resources, Writing – Review & Editing, Supervision; **L.E. Fratila-Apachitei**: Methodology, Resources, Writing – Review & Editing, Supervision; **J.M.C. Mol**: Methodology, Resources, Writing – Review & Editing, Supervision; **J. Zhou**: Conceptualization, Methodology, Resources, Writing – Review & Editing, Supervision; **A.A. Zadpoor**: Conceptualization, Resources, Writing – Review & Editing, Supervision, Funding Acquisition.

Declaration of competing interest

The authors declare that they have no known competing financial interests or personal relationships that could have appeared to influence the work reported in this paper.

Acknowledgments

This work is part of the 3DMed project that has received the funding from the Interreg 2 Seas program 2014–2020, co-funded by the European Regional Development Fund under subsidy contract No. 2S04-014. Mr. Ruud Hendrikx at the Department of Materials Science and Engineering, Delft University of Technology is acknowledged for the XRD analysis. Mr. Michel van den Brink at the Department of Process and Energy, Delft University of Technology is acknowledged for the ICP-OES analysis.

Appendix A. Supplementary data

Supplementary data to this article can be found online at https://doi.org/10.1016/j.msec.2021.112617.

References

[1] R. Gorejová, L. Haverová, R. Oriňaková, A. Oriňak, M. Oriňak, Recent advancements in Fe-based biodegradable materials for bone repair, J. Mater. Sci. 54 (2019) 1913–1947, https://doi.org/10.1007/s10853-018-3011-z.

[2] C. Shuai, S. Li, S. Peng, P. Feng, Y. Lai, C. Gao, Biodegradable metallic bone implants, Mater. Chem. Front. 3 (2019) 544–562, https://doi.org/10.1039/c8qm00507a.

[3] J. He, F.L. He, D.W. Li, Y.L. Liu, Y.Y. Liu, Y.J. Ye, D.C. Yin, Advances in Fe-based biodegradable metallic materials, RSC Adv. 6 (2016) 112819–112838, https://doi.org/10.1039/C6RA20594A.

[4] T. Kraus, F. Moszner, S. Fischerauer, M. Fiedler, E. Martinelli, J. Eichler, F. Witte, E. Willbold, M. Schinhammer, M. Meischel, P.J. Uggowitzer, J.F. Löffler, A. Weinberg, Biodegradable Fe-based alloys for use in osteosynthesis: outcome of an in vivo study after 52 weeks, Acta Biomater. 10 (2014) 3346–3353, https://doi.org/10.1016/j.actbio.2014.04.007.

[5] E. Zhang, H. Chen, F. Shen, Biocorrosion properties and blood and cell compatibility of pure iron as a biodegradable biomaterial, J. Mater. Sci. Mater. Med. 21 (2010) 2151–2163, https://doi.org/10.1007/s10856-010-4070-0.

[6] D. Xia, F. Yang, Y. Zheng, Y. Liu, Y. Zhou, Research status of biodegradable metals designed for oral and maxillofacial applications: a review, Bioact. Mater. 6 (2021) 4186–4208, https://doi.org/10.1016/j.bioactmat.2021.01.011.

[7] Y.F. Zheng, X.N. Gu, F. Witte, Biodegradable metals, Mater. Sci. Eng. R 77 (2014) 1–34, https://doi.org/10.1007/978-1-4614-3942-4_5.

[8] M. Schinhammer, A.C. Hänzi, J.F. Löffler, P.J. Uggowitzer, Design strategy for biodegradable Fe-based alloys for medical applications, Acta Biomater. 6 (2010) 1705–1713, https://doi.org/10.1016/j.actbio.2009.07.039.

[9] K. Munir, A. Biesiekierski, C. Wen, Y. Li, Biodegradable alloys, Struct. Biomater. - Prop. Charact. Sel, Woodhead Publishing 2021, pp. 189–228, https://doi.org/10.1016/b978-0-12-818831-6.00001-x.

[10] Y. Li, H. Jahr, K. Lietaert, P. Pavanram, A. Yilmaz, L.I. Fockaert, M.A. Leeflang, B. Pouran, Y. Gonzalez-Garcia, H. Weinans, J.M.C. Mol, J. Zhou, A.A. Zadpoor, Additively manufactured biodegradable porous iron, Acta Biomater. 77 (2018) 380–393, https://doi.org/10.1016/j.actbio.2018.07.011.

[11] D. Carluccio, C. Xu, J. Venezuela, Y. Cao, D. Kent, M. Bermingham, A.G. Demir, B. Previtali, Q. Ye, M. Dargusch, Additively manufactured iron-manganese for biodegradable porous load-bearing bone scaffold applications, Acta Biomater. 103 (2020) 346–360, https://doi.org/10.1016/j.actbio.2019.12.018.

[12] C. Shuai, W. Yang, Y. Yang, H. Pan, C. He, F. Qi, D. Xie, H. Liang, Selective laser melted fe-mn bone scaffold: microstructure, corrosion behavior and cell response, Mater. Res. Express. 7 (2019), 015404, https://doi.org/10.1088/2053-1591/ab62f5.

[13] N.E. Putra, M.A. Leeflang, M. Minneboo, P. Taheri, L.E. Fratila-Apachitei, J.M.C. Mol, J. Zhou, A.A. Zadpoor, Extrusion-based 3D printed biodegradable porous iron, Acta Biomater. 121 (2021) 741–756, https://doi.org/10.1016/j.actbio.2020.11.022.

[14] R. Oriňaková, R. Gorejová, Z. Orságová Králová, A. Oriňak, Surface modifications of biodegradable metallic foams for medical applications, Coatings 10 (2020) 819, https://doi.org/10.3390/coatings10090819.

[15] A.H. Yusop, A. Al Sakkaf, H. Nur, Modifications on porous absorbable fe-based scaffolds for bone applications : a review from corrosion and biocompatibility viewpoints, J. Biomed. Mater. Res. Part B Appl. Biomater. (2021) 1–27, https://doi.org/10.1002/jbm.b.34893.

[16] H. Chen, E. Zhang, K. Yang, Microstructure, corrosion properties and bio-compatibility of calcium zinc phosphate coating on pure iron for biomedical application, Mater. Sci. Eng. C. 34 (2014) 201–206, https://doi.org/10.1016/j.msec.2013.09.010.

[17] N. Mohd Daud, N.B. Sing, A.H. Yusop, F.A. Abdul Majid, H. Hermawan, Degradation and in vitro cell-material interaction studies on hydroxyapatite-coated biodegradable porous iron for hard tissue scaffolds, J. Orthop. Transl. 2 (2014) 177–184, https://doi.org/10.1016/j.jot.2014.07.001.

[18] A. Adhilakshmi, K. Ravichandran, T.S.N. Sankara Narayanan, Protecting electrochemical degradation of pure iron using zinc phosphate coating for biodegradable implant applications, New J. Chem. 42 (2018) 18458–18468, https://doi.org/10.1039/c8nj02986e.

[19] Y. Su, S. Champagne, A. Trenggono, R. Tolouei, D. Mantovani, H. Hermawan, Development and characterization of silver containing calcium phosphate coatings on pure iron foam intended for bone scaffold applications, Mater. Des. 148 (2018) 124–134, https://doi.org/10.1016/j.matdes.2018.03.061.

[20] M. Hrubovčáková, M. Kupková, M. Džupon, M. Giretová, L. Medvecký, R. Džunda, Biodegradable polylactic acid and polylactic acid/hydroxyapatite coated iron foams for bone replacement materials, Int. J. Electrochem. Sci. 12 (2017) 11122–11136, https://doi.org/10.20964/2017.12.53.

[21] Y. Qi, H. Qi, Y. He, W. Lin, P. Li, L. Qin, Y. Hu, L. Chen, Q. Liu, H. Sun, Q. Liu, G. Zhang, S. Cui, J. Hu, L. Yu, D. Zhang, J. Ding, Strategy of metal-polymer composite stent to accelerate biodegradation of iron-based biomaterials, ACS Appl. Mater. Interfaces 10 (2018) 182–192, https://doi.org/10.1021/acsami.7b15206.

[22] X. Li, W. Zhang, W. Lin, H. Qiu, Y. Qi, X. Ma, H. Qi, Y. He, H. Zhang, J. Qian, G. Zhang, R. Gao, D. Zhang, J. Ding, Long-term efficacy of biodegradable metal-polymer composite stents after the first and the second implantations into porcine coronary arteries, ACS Appl. Mater. Interfaces 12 (2020) 15703–15715, https://doi.org/10.1021/acsami.0c00971.

[23] A.H.M. Yusop, N.M. Daud, H. Nur, M.R.A. Kadir, H. Hermawan, Controlling the degradation kinetics of porous iron by poly(lactic-co-glycolic acid) infiltration for use as temporary medical implants, Sci. Rep. 5 (2015) 1–17, https://doi.org/10.1038/srep11194.

[24] L. Haverová, R. Oriňaková, A. Oriňak, R. Gorejová, M. Baláž, P. Vanýsek, M. Kupková, M. Hrubovčáková, P. Mudroň, J. Radoňák, Z.O. Králová, A.M. Turoňová, An in vitro corrosion study of open cell iron structures with PEG coating for bone replacement applications, Metals (Basel) 8 (2018) 1–21, https://doi.org/10.3390/met8070499.

[25] R. Gorejová, R. Oriňaková, Z. Orságová Králová, M. Baláž, M. Kupková, M. Hrubovčáková, L. Haverová, M. Džupon, A. Oriňak, F. Kaľavský, K. Kovaľ, In vitro corrosion behavior of biodegradable iron foams with polymeric coating, Materials (Basel) 13 (2020) 1–17.

[26] J.Z. Wang, M.L. You, Z.Q. Ding, W. Bin Ye, A review of emerging bone tissue engineering via PEG conjugated biodegradable amphiphilic copolymers, Mater. Sci. Eng. C. 97 (2019) 1021–1035, https://doi.org/10.1016/j.msec.2019.01.057.

[27] S. Jin, X. Xia, J. Huang, C. Yuan, Y. Zuo, Y. Li, J. Li, Recent advances in PLGA-based biomaterials for bone tissue regeneration, Acta Biomater. 127 (2021) 56–79, https://doi.org/10.1016/j.actbio.2021.03.067.

[28] R. Baptista, M. Guedes, Morphological and mechanical characterization of 3D printed PLA scaffolds with controlled porosity for trabecular bone tissue replacement, Mater. Sci. Eng. C 118 (2021), 111528, https://doi.org/10.1016/j.msec.2020.111528.

[29] C.W. McGary Jr., Degradation of poly(ethylene oxide), J. Polym. Sci. 46 (1960) 51–57, https://doi.org/10.1002/pol.1960.1204614705.

[30] V.R. De La Rosa, Poly(2-oxazoline)s as materials for biomedical applications, J. Mater. Sci. Mater. Med. 25 (2014) 1211–1225, https://doi.org/10.1007/s10856-013-5034-y.

[31] T. Lorson, M.M. Lübtow, E. Wegener, M.S. Haider, S. Borova, D. Nahm, R. Jordan, M. Sokolski-Papkov, A.V. Kabanov, R. Luxenhofer, Poly(2-oxazoline)s based biomaterials: a comprehensive and critical update, Biomaterials 178 (2018) 204–280, https://doi.org/10.1016/j.biomaterials.2018.05.022.

[32] H.P.C. Van Kuringen, J. Lenoir, E. Adriaens, J. Bender, B.G. De Geest, R. Hoogenboom, Partial hydrolysis of poly(2-ethyl-2-oxazoline) and potential implications for biomedical applications? Macromol. Biosci. 12 (2012) 1114–1123, https://doi.org/10.1002/mabi.201200080.

[33] B. Pidhatika, M. Rodenstein, Y. Chen, E. Rakhmatullina, A. Mühlebach, C. Acikgöz, M. Textor, R. Konradi, Comparative stability studies of Poly(2-methyl-2-oxazoline) and Poly(ethylene glycol) brush coatings, Biointerphases 7 (2012) 1–4, https://doi.org/10.1007/s13758-011-0001-y.

[34] T.R. Dargaville, B.G. Hollier, A. Shokoohmand, R. Hoogenboom, Poly(2-oxazoline) hydrogels as next generation three-dimensional cell supports, Cell Adhes. Migr. 8 (2014) 88–93, https://doi.org/10.4161/cam.28205.

[35] O. Sedlacek, R. Hoogenboom, Drug delivery systems based on poly(2-oxazoline)s and poly(2-oxazine)s, Adv. Ther. 3 (2020) 1900168, https://doi.org/10.1002/adtp.201900168.

[36] Y. You, K. Kobayashi, B. Colak, P. Luo, E. Cozens, L. Fields, K. Suzuki, J. Gautrot, Engineered cell-degradable poly(2-alkyl-2-oxazoline) hydrogel for epicardial placement of mesenchymal stem cells for myocardial repair, Biomaterials 269 (2021), 120356, https://doi.org/10.1016/j.biomaterials.2020.120356.

[37] V.R. De La Rosa, S. Tempelaar, P. Dubois, R. Hoogenboom, L. Mespouille, Poly(2-ethyl-2-oxazoline)-block-polycarbonate block copolymers: from improved end-group control in poly(2-oxazoline)s to chain extension with aliphatic polycarbonate through a fully metal-free ring-opening polymerisation process, Polym. Chem. 7 (2016) 1559–1568, https://doi.org/10.1039/c5py01913c.

[38] ASTM B963-17, Standard test methods for oil content, oil-impregnation efficiency, and surface-connected porosity of sintered powder metallurgy (PM) products using Archimedes' principle, J. ASTM Int. (2017), https://doi.org/10.1520/B0963-14.

[39] A. Oyane, H. Kim, T. Furuya, T. Kokubo, T. Miyazaki, T. Nakamura, Preparation and assessment of revised simulated body fluids, J. Biomed. Mater. Res. A 65 (2003) 188–195, https://doi.org/10.1002/jbm.a.10482.

[40] L. Yang, E. Zhang, Biocorrosion behavior of magnesium alloy in different simulated fluids for biomedical application, Mater. Sci. Eng. C. 29 (2009) 1691–1696, https://doi.org/10.1016/j.msec.2009.01.014.

[41] ASTM G1-03, Standard practice for preparing, cleaning, and evaluating corrosion test, J. ASTM Int. (2017), https://doi.org/10.1520/G0001-03R11.

[42] ASTM G31-72, Standard practice for laboratory immersion corrosion testing for metals, J. ASTM Int. (2004)https://doi.org/10.1520/G0031-72R04.

[43] ISO 13314, Mechanical testing of metals - Ductility testing - Compression test for porous and cellular metals, International Organization for Standardization, 2011 doi:ISO 13314:2011.

[44] ISO 10993-12, Sample preparation and reference materials, International Organization for Standardization, 2012, https://doi.org/10.1016/S0080-8784(08)60069-1.

[45] A. Colombo, F. Gherardi, S. Goidanich, J.K. Delaney, E.R. De La Rie, M.C. Ubaldi, L. Toniolo, R. Simonutti, Highly transparent poly(2-ethyl-2-oxazoline)-TiO2 nanocomposite coatings for the conservation of matte painted artworks, RSC Adv. 5 (2015) 84879–84888, https://doi.org/10.1039/c5ra10895k.

[46] E.D.H. Mansfield, K. Sillence, P. Hole, A.C. Williams, V.V. Khutoryanskiy, POZylation: a new approach to enhance nanoparticle diffusion through mucosal barriers, Nanoscale 7 (2015) 13671–13679, https://doi.org/10.1039/c5nr03178h.

[47] G.K. Abilova, D.B. Kaldybekov, E.K. Ozhmukhametova, A.Z. Saimova, D.S. Kazybayeva, G.S. Irmukhametova, V.V. Khutoryanskiy, Chitosan/poly(2-ethyl-2-oxazoline) films for ocular drug delivery: formulation, miscibility, in vitro and in vivo studies, Eur. Polym. J. 116 (2019) 311–320, https://doi.org/10.1016/j.eurpolymj.2019.04.016.

[48] E.F. Morgan, G.U. Unnikrisnan, A.I. Hussein, Bone mechanical properties in healthy and diseased states, Annu. Rev. Biomed. Eng. 20 (2018) 119–143, https://doi.org/10.1146/annurev-bioeng-062117-121139.

[49] K. Gulati, S. Ramakrishnan, M.S. Aw, G.J. Atkins, D.M. Findlay, D. Losic, Biocompatible polymer coating of titania nanotube arrays for improved drug elution and osteoblast adhesion, Acta Biomater. 8 (2012) 449–456, https://doi.org/10.1016/j.actbio.2011.09.004.

[50] I.A. Neacşu, A.I. Nicoară, O.R. Vasile, B.Ş. Vasile, Inorganic micro- and nanostructured implants for tissue engineering, Nanobiomaterials Hard Tissue Eng. Appl. Nanobiomaterials. (2016) 271–295, https://doi.org/10.1016/B978-0-323-42862-0.00009-2.

[51] S. Julmi, A.K. Krüger, A.C. Waselau, A. Meyer-Lindenberg, P. Wriggers, C. Klose, H.J. Maier, Processing and coating of open-pored absorbable magnesium-based bone implants, Mater. Sci. Eng. C 98 (2019) 1073–1086, https://doi.org/10.1016/j.msec.2018.12.125.

[52] P. Taheri, J. Wielant, T. Hauffman, J.R. Flores, F. Hannour, J.H.W. De Wit, J.M.C. Mol, H. Terryn, A comparison of the interfacial bonding properties of carboxylic acid functional groups on zinc and iron substrates, Electrochim. Acta 56 (2011) 1904–1911, https://doi.org/10.1016/j.electacta.2010.10.079.

[53] C.S. Obayi, R. Tolouei, C. Paternoster, S. Turgeon, B.A. Okorie, D.O. Obikwelu, G. Cassar, J. Buhagiar, D. Mantovani, Influence of cross-rolling on the micro-texture and biodegradation of pure iron as biodegradable material for medical implants, Acta Biomater. 17 (2015) 68–77, https://doi.org/10.1016/j.actbio.2015.01.024.

[54] Y. Li, H. Jahr, P. Pavanram, F.S.L. Bobbert, U. Puggi, X.Y. Zhang, B. Pouran, M.A. Leeflang, H. Weinans, J. Zhou, A.A. Zadpoor, Additively manufactured functionally graded biodegradable porous iron, Acta Biomater. 96 (2019) 646–661, https://doi.org/10.1016/j.actbio.2019.07.013.
[55] N.E. Putra, M.A. Leeflang, P. Taheri, L.E. Fratila-Apachitei, J.M.C. Mol, J. Zhou, A.A. Zadpoor, Extrusion-based 3D printing of ex situ-alloyed highly biodegradable MRI-friendly porous iron-manganese scaffolds, Acta Biomater. 134 (2021) 774–990, https://doi.org/10.1016/j.actbio.2021.07.042.
[56] A. Drynda, T. Hassel, F.W. Bach, M. Peuster, In vitro and in vivo corrosion properties of new iron-manganese alloys designed for cardiovascular applications, J. Biomed. Mater. Res. B Appl. Biomater. 103 (2015) 649–660, https://doi.org/10.1002/jbm.b.33234.
[57] H. Liu, H. Yazici, C. Ergun, T.J. Webster, H. Bermek, An in vitro evaluation of the Ca/P ratio for the cytocompatibility of nano-to-micron particulate calcium phosphates for bone regeneration, Acta Biomater. 4 (2008) 1472–1479, https://doi.org/10.1016/j.actbio.2008.02.025.
[58] T.X. Viegas, M.D. Bentley, J.M. Harris, Z. Fang, K. Yoon, B. Dizman, R. Weimer, A. Mero, G. Pasut, F.M. Veronese, Polyoxazoline: chemistry, properties, and applications in drug delivery, Bioconjug. Chem. 22 (2011) 976–986, https://doi.org/10.1021/bc200049d.
[59] J. Ulbricht, R. Jordan, R. Luxenhofer, On the biodegradability of polyethylene glycol, polypeptoids and poly(2-oxazoline)s, Biomaterials 35 (2014) 4848–4861, https://doi.org/10.1016/j.biomaterials.2014.02.029.
[60] J. Ulbricht, Insights into polymer biodegradation: Investigations on oxidative, hydrolytic and enzymatic pathways, Universität Würzburg, 2018 Doctoral Thesis.
[61] D. You, N. Pebere, F. Dabosi, An investigation of the corrosion of pure iron by electrochemical techniques and in situ observations, Corros. Sci. 34 (1993) 5–15, https://doi.org/10.1016/0010-938X(93)90254-E.
[62] T. Chen, H. Huang, H. Ma, D. Kong, Effects of surface morphology of nanostructured PbO2 thin films on their electrochemical properties, Electrochim. Acta 88 (2013) 79–85, https://doi.org/10.1016/j.electacta.2012.10.009.
[63] S. Skale, V. Doleček, M. Slemnik, Electrochemical impedance studies of corrosion protected surfaces covered by epoxy polyamide coating systems, Prog. Org. Coat. 62 (2008) 387–392, https://doi.org/10.1016/j.porgcoat.2008.02.003.
[64] R. Oriňaková, R. Gorejová, Z. Orságová Králová, L. Haverová, A. Oriňak, I. Maskaľová, M. Kupková, M. Džupon, M. Baláž, M. Hrubovčáková, T. Sopčák, A. Zubrik, M. Oriňak, Evaluation of mechanical properties and hemocompatibility of open cell iron foams with polyethylene glycol coating, Appl. Surf. Sci. 505 (2020), 144634, https://doi.org/10.1016/j.apsusc.2019.144634.
[65] A. Sharma, M.C. Oh, B. Ahn, Recent advances in very high cycle fatigue behavior of metals and alloys—a review, Metals (Basel) 10 (2020) 1–23, https://doi.org/10.3390/met10091200.
[66] A. Yamamoto, R. Honma, M. Sumita, Cytotoxicity evaluation of 43 metal salts using murine fibroblasts and osteoblastic cells, J. Biomed. Mater. Res. 39 (1998) 331–340, https://doi.org/10.1002/(SICI)1097-4636(199802)39:2<331::AID-JBM22>3.0.CO;2-E.
[67] ISO 10993-5, Tests for in vitro cytotoxicity, International Organization for Standardization, 2009, https://doi.org/10.1021/es0620181.
[68] Y.F. He, Y. Ma, C. Gao, G.Y. Zhao, L.L. Zhang, G.F. Li, Y.Z. Pan, K. Li, Y.J. Xu, Iron overload inhibits osteoblast biological activity through oxidative stress, Biol. Trace Elem. Res. 152 (2013) 292–296, https://doi.org/10.1007/s12011-013-9605-z.
[69] R. Oriňaková, R. Gorejová, Z.O. Králová, A. Oriňak, I. Shepa, J. Hovancová, A. Kovalčíková, Z.L. Bujňáková, N. Király, M. Kaňuchová, M. Baláž, M. Strečková, M. Kupková, M. Hrubovčáková, F. Kaľavský, M. Oriňak, Influence of albumin interaction on corrosion resistance of sintered iron biomaterials with polyethyleneimine coating, Appl. Surf. Sci. 509 (2020), 145379, https://doi.org/10.1016/j.apsusc.2020.145379.
[70] J. Wei, T. Igarashi, N. Okumori, T. Igarashi, T. Maetani, B. Liu, M. Yoshinari, Influence of surface wettability on competitive protein adsorption and initial attachment of osteoblasts, Biomed. Mater. 4 (2009), 045002, https://doi.org/10.1088/1748-6041/4/4/045002.
[71] E.A. Dos Santos, M. Farina, G.A. Soares, K. Anselme, Surface energy of hydroxyapatite and β-tricalcium phosphate ceramics driving serum protein adsorption and osteoblast adhesion, J. Mater. Sci. Mater. Med. 19 (2008) 2307–2316, https://doi.org/10.1007/s10856-007-3347-4.
[72] V. Wagener, A.S. Faltz, M.S. Killian, P. Schmuki, S. Virtanen, Protein interactions with corroding metal surfaces: comparison of Mg and Fe, Faraday Discuss. 180 (2015) 347–360, https://doi.org/10.1039/c4fd00253a.
[73] R. Eid, N.T.T. Arab, M.T. Greenwood, Iron mediated toxicity and programmed cell death: a review and a re-examination of existing paradigms, Biochim. Biophys. Acta Mol. Cell Res. 2017 (1864) 399–430, https://doi.org/10.1016/j.bbamcr.2016.12.002.
[74] R. Oriňaková, R. Gorejová, J. Macko, A. Oriňak, M. Kupková, M. Hrubovčáková, J. Ševc, R.M. Smith, Evaluation of in vitro biocompatibility of open cell iron structures with PEG coating, Appl. Surf. Sci. 475 (2019) 515–518, https://doi.org/10.1016/j.apsusc.2019.01.010.
[75] S. Huang, A. Ulloa, E. Nauman, L. Stanciu, Collagen coating effects on Fe–Mn bioresorbable alloys, J. Orthop. Res. 38 (2020) 523–535, https://doi.org/10.1002/jor.24492.
[76] F. Pluronic, Y. Hwang, P. Chiang, W. Hong, C. Chiao, I. Chu, Study in vivo intraocular biocompatibility of in situ gelation hydrogels: poly(2-ethyl oxazoline)-block-poly(e-caprolactone)-block-Poly(2-ethyl oxazoline) copolymer, matrigel and pluronic F127, PLoS One 8 (2013) 1–9, https://doi.org/10.1371/journal.-pone.0067495.
[77] J. Tong, X. Yi, R. Luxenhofer, W.A. Banks, R. Jordan, M.C. Zimmerman, A.V. Kabanov, Conjugates of superoxide dismutase 1 with amphiphilic poly(2-oxazoline) block copolymers for enhanced brain delivery: synthesis, characterization and evaluation in vitro and in vivo, Mol. Pharm. 10 (2013) 360–377, https://doi.org/10.1021/mp300496x.
[78] H. Ma, T. Li, Z. Huan, M. Zhang, Z. Yang, J. Wang, J. Chang, C. Wu, 3D printing of high-strength bioscaffolds for the synergistic treatment of bone cancer, NPG Asia Mater. 10 (2018) 31–44, https://doi.org/10.1038/s41427-018-0015-8.
[79] C. Shuai, Y. Li, Y. Yang, S. Peng, W. Yang, F. Qi, S. Xiong, H. Liang, L. Shen, Bioceramic enhances the degradation and bioactivity of iron bone implant, Mater. Res. Express. 6 (2019), 115401, https://doi.org/10.1088/2053-1591/ab45b9.
[80] C. Gao, M. Yao, S. Li, P. Feng, S. Peng, C. Shuai, Highly biodegradable and bioactive fe-pd-bredigite biocomposites prepared by selective laser melting, J. Adv. Res. 20 (2019) 91–104, https://doi.org/10.1016/j.jare.2019.06.001.